HOT BOTTOM BURNING IN INTERMEDIATE MASS STARS

JOHN LATTANZIO[1,2], CHERYL FROST[1,2], ROBERT CANNON[2,3], PETER WOOD[4]
[1] *Monash University, Melbourne, Australia*
[2] *Institute of Astronomy, Cambridge, England*
[3] *Southhampton University, Southhampton, England*
[4] *Mt Stromlo Observatory, Canberra, Australia*

ABSTRACT. We discuss nucleosynthesis within intermediate mass stars by considering a $6\,M_\odot$ model with $Z = 0.02$ as a typical example. The emphasis is on the AGB phase of evolution, with particular reference to nuclear burning in the bottom of the convective envelope. We find strong CN cycling, with substantial Al production. Further we confirm previous calculations of lithium production, and show that this model should produce Fl depletions rather than enhancements.

1. Background and Motivation

Our knowledge of the AGB phase of evolution has increased dramatically over the last decade or so. This has been driven primarily by observational studies, with theory lagging somewhat behind. An area where theoretical studies are desperately needed is in quantifying the nucleosynthesis which occurs in intermediate mass stars during their thermally pulsing evolution. While there are many calculations of the thermal pulses themselves, and associated dredge-up, there are few calculations which include a large nucleosynthesis network, or which include the recently discovered "Hot Bottom Burning".

Hot Bottom Burning (hereafter HBB) is the colourful name given to the circumstance where the bottom of the convective envelope of a star reaches temperatures sufficiently high for significant nucleosynthesis to take place. It is perhaps better to think of this as the bottom of the envelope reaching into the top of the hydrogen shell, although the two are of course equivalent, due to the monotonic variation of temperature within the star (at least in this region). Thus there is a thin layer at high temperatures, and material is mixed through this region and then into the outer envelope where the lower temperatures shutdown any nuclear processing which may occur at the deepest points in the envelope. For nuclear reactions with time-scales similar to (or shorter than) the mixing time-scale, we cannot make the usual assumption of instantaneous mixing at an average burning rate.

The historical motivation for realising the importance of HBB can be briefly summarised thus: When the brightest AGB stars in the Magellanic Clouds were observed by Wood, Bessell and Fox (1983) they were surprised to discover that they were not carbon stars. Thus they suggested that perhaps the carbon dredged to their surface after thermal pulses had been burned, by HBB, into ^{13}C and ^{14}N. Further observations of these stars by Smith and Lambert (1989) showed that they were also super-rich in ^{7}Li. This was taken as evidence for the "Beryllium transport mechanism", proposed by Cameron and Fowler (1971), which requires high temperatures at the bottom of a deep convective envelope. The inescapable conclusion was that HBB was responsible for the unusual envelope composition of these stars. Quantitative theoretical studies by Boothroyd and Sackmann (1992) showed that the models could indeed match the observations. In the meantime, ion-probe studies of meteorites were revealing unusual isotopic compositions in some grains (such as SiC) which were almost certainly formed in the envelopes of AGB stars. Some corundum (Al_2O_3) grains showed large enhancements of ^{26}Al, which was taken as evidence for high temperature hydrogen burning in a region with $C/O < 1$, as expected in these intermediate mass stars with HBB. The evidence for the occurrence of HBB was very strong, but there were only limited calculations available, mostly focusing on ^{7}Li. It is our aim to study the detailed nucleosynthesis occurring in these stars by combining a detailed nuclear reaction network with an algorithm for time-dependent convection, as discussed below.

2. Method and Requirements

Such a study requires us to combine detailed nucleosynthesis with detailed evolution models. We have chosen to do this with two separate calculations. Firstly, we perform the evolutionary calculations. Following this, a nucleosynthesis code is used to calculate the detailed nuclear burning and composition profiles for models with the structure previously calculated by the evolution code. The compositions calculated by the two codes are completely independent, and the agreement between the two serves as a consistency check. The agreement has always been to within a few percent.

The evolution is calculated with the Mt Stromlo evolution code, modified to include the OPAL opacities (Rogers and Iglesias 1992). This evolution is calculated in the usual way, and with only seven independent nuclear species. This is possible because the species important to the evolution are only those whose burning provides input for the structure calculation. Also, we make the usual assumption of instantaneous mixing within convection zones. We address the problem of extra-mixing at the edge of the convective envelope during dredge-up by using a simple method which involves the extrapolation of the ratio of the radiative to adiabatic gradients, as discussed in Lattanzio (1986). We also include the entropy adjustment due to dredge-up in the way discussed by Wood (1981). For a detailed discussion of the sensitivity of dredge-up to details of the calculations, we refer the reader to Frost and Lattanzio (1996a).

With these ingredients we calculate the evolution of our stellar models, from contraction to the ZAMS through to the thermally pulsing evolution on the AGB. Throughout, we output the structure of the model every so often, to be used as input for the nucleosynthesis calculation. The calculations reported here are for a nuclear reaction network of 506 reaction for 74 species up to ^{35}S, and including a small iron-group network consisting of $^{56-61}$Fe, $^{59-61}$Co, and $^{58-62}$Ni. To simulate the neutron capture on species not included we alter the ^{35}S neutron capture cross-section in the same way as outlined by Jorissen and Arnould (1989). We also add the fictional particle g, to count the number of neutron captures occurring beyond ^{62}Ni. This is done via the fictional reaction

$$^{62}\mathrm{Ni} + \mathrm{n} \rightarrow {}^{62}\mathrm{Ni} + \mathrm{g}.$$

Thus the sum of the number of g's present indicates the approximate number of neutron captures occurring on heavier elements not included in our calculation.

The nucleosynthesis code is based on that used by Cannon (1993) for the study of Thorne-Źytkow objects, but with substantial modifications. The inputs for the calculation are the temperature, density, radius, mixing-length and mixing velocity as a function of mass within the model. Between evolution models the nucleosynthesis code creates its own mass mesh, based on accurate resolution of regions undergoing rapid composition change. We use a combination of Lagrangian points (in radiative zones where there is minimal burning) and non-Lagrangian points. The latter are divided into three cases. In the convective envelope the position in mass of the outer points follows the mass-loss, whereas the inner points follow the advancement of the hydrogen shell. Finally, in a nuclear burning shell we move the points in a self-similar fashion, using the position of the hydrogen shell as determined by the evolution calculation. This again serves as a consistency check: if the shell does not evolve at the same rate in both codes then the position of the shell in the codes will not agree. This is the only time that abundances from the evolutionary calculation are used in the post-processing code: to set up the mesh for the shell advancement. Further, special attention is paid to maintaining convective and compositional boundaries during all phases, especially dredge-up and shell re-ignition. Nuclear reaction rates are primarily taken from the data base of Thielemann et al (1987). There are some notable exceptions, such as the recent alpha-particle capture rate for ^{18}O (Käppeler et al 1994). Further details of both the code and the nuclear reaction rates may be found in Cannon et al (1996).

At this workshop we present a summary of results for a 6 $\mathrm{M}_\odot$ model (from here on we measure all masses in solar units with solar composition $Z = 0.02$. This mass was chosen because it is expected to show HBB, and hence to illustrate the kind of features we are hoping to investigate with our project. Subsequent calculations will extend the mass and composition range, and further details of this calculation can be found in Cannon et al (1996).

3. Pre-AGB Evolution

The evolution of our stellar model is qualitatively well understood, and we do not give details here. Rather, we concentrate on the compositions, which are most relevant for our present purposes.

3.1. Core Hydrogen Burning and First Dredge-Up

Core hydrogen exhaustion occurs after some 5.1×10^7 years. The composition at this point is shown in Figure 1, and we see the usual variations. Moving inward from the surface, the increasing temperature starts the CN cycle, so we see an increase in ^{13}C at the cost of ^{12}C. In this same region (between $M = 3$ and 4) we see a decrease in the ^{15}N due to ^{15}N(p,α)^{12}C, and then a slight increase due to ^{18}O(p,α)^{15}N. Just slightly

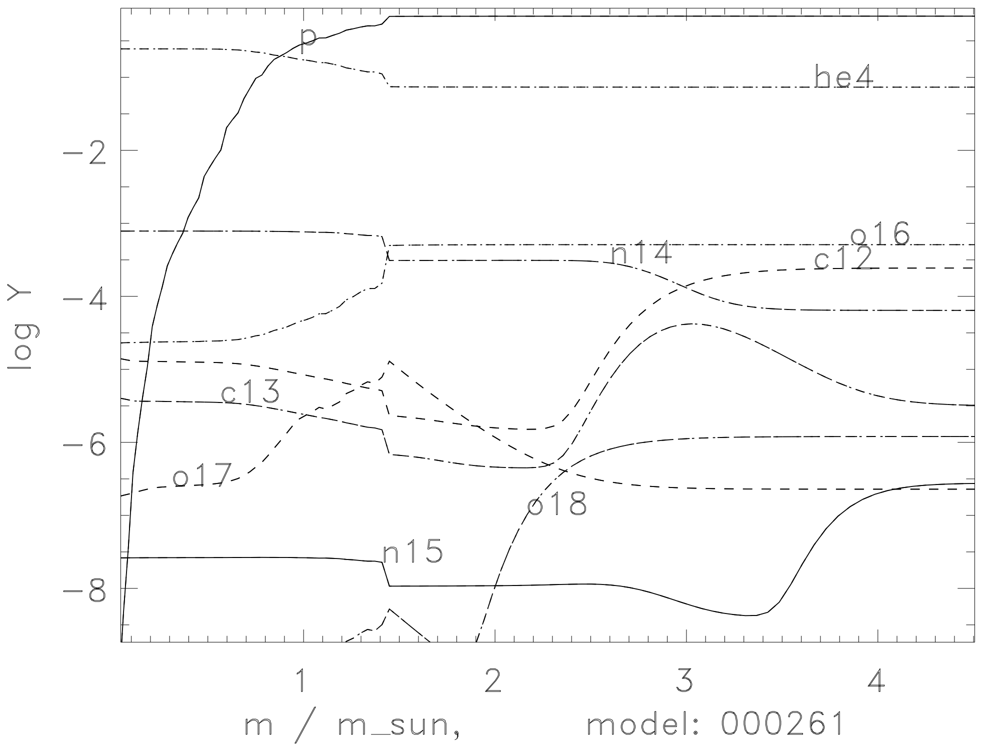

Fig. 1. Composition profiles at the time of core hydrogen exhaustion. Note that during first dredge-up the convective envelope will reach down to $M = 1.256$, thus homogenising the material from that point to the surface.

interior to $M = 3$ the ^{13}C is itself destroyed in the production of ^{14}N, which now starts to rise. From here inwards the carbon isotopes are in equilibrium. Interior to $M \simeq 2.5$ we see substantial destruction of ^{18}O from the proton captures described above. At $M \simeq 1.8$ we see the production of ^{17}O from proton captures on ^{16}O, as the ON cycle starts to function more strongly (although it never reaches equilibrium in this star, whose central burning occurs at a temperature of about 30×10^6K). The discontinuity in the abundance profiles at $M = 1.5$ reflects the maximum size of the convective core during hydrogen burning. As the hydrogen content of the convective core decreases, so too does the extent of the convective core, and this is seen in many of the abundance profiles in Figure 1.

Not shown in the figure are the Ne-Na and Mg-Al isotope abundances. Briefly, there is essentially no change in the abundance ^{20}Ne, but we see an increase of ^{21}Ne at relatively low temperatures (between $M = 0.8$ and 1.5) and a decrease interior to that. In the region of the erstwhile convective core all of the ^{22}Ne has been destroyed by proton

TABLE 1

Ratio	Initial Value	First Dredge-Up	Second Dredge-Up
^{12}C / ^{13}C	90	19.3	18.0
^{14}N / ^{15}N	273	1297	1931
^{16}O / ^{17}O	2632	453	408
^{16}O / ^{18}O	500	562	572

Various abundance ratios for the evolution described in the text. We give the initial value as well as the values after both the first and second dredge-up.

captures, producing a 0.8 dex increase in the abundance of ^{23}Na. For the Mg-Al cycle, there is no change of the ^{24}Mg content, but a decrease of ^{25}Mg by just over 1 dex, and an increase in ^{26}Mg by about a factor of 2. These results are as expected for burning at $T \simeq 30 \times 10^6$K (e.g. Arnould, Mowlavi and Champagne 1996).

As the star ascends the giant branch for the first time the convective envelope reaches down to $M = 1.256$ with consequent homogenisation of the abundances from this point outward. This is known as the First Dredge-Up episode, and the key abundance changes are listed in Table 1.

3.2. Core Helium Burning and Second Dredge-Up

Once helium is ignited in the core the star has two energy sources: the hydrogen shell and the helium core. The compositions at this stage are shown in Figure 2.

Firstly, within the helium core, the nucleosynthesis is relatively simple. Primarily we have the triple-alpha reactions providing ^{12}C and then further alpha captures giving ^{16}O. Also, the large amount of ^{14}N left over from CNO cycling means that $^{14}\mathrm{N}(\alpha,\gamma)^{18}\mathrm{F}(\beta^+\nu)^{18}\mathrm{O}$ produces a fairly large amount of ^{18}O. This ^{18}O is also capable of alpha-capture which produces ^{22}Ne which produces some neutrons via $^{22}\mathrm{Ne}(\alpha,\mathrm{n})^{25}\mathrm{Mg}$.

Moving to hydrogen shell burning, we see the usual signature of the CNO cycles, with CN running in equilibrium. ^{18}O is virtually completely destroyed, while ^{17}O maintains a small presence due to proton captures on the abundant ^{16}O. The destruction of the ^{18}O via (p,α) produces ^{15}N, but this is also destroyed by (p,α) to finally feed back into ^{12}C, thus keeping the ^{15}N abundance low.

The nucleosynthesis in the intermediate region, between the hydrogen "exhausted" region and the edge of the convective helium core is somewhat easier to see here because the temperature gradient separates different reactions and the lack of convection maintains the profiles which were homogenised in the convective core. Hence, just outside

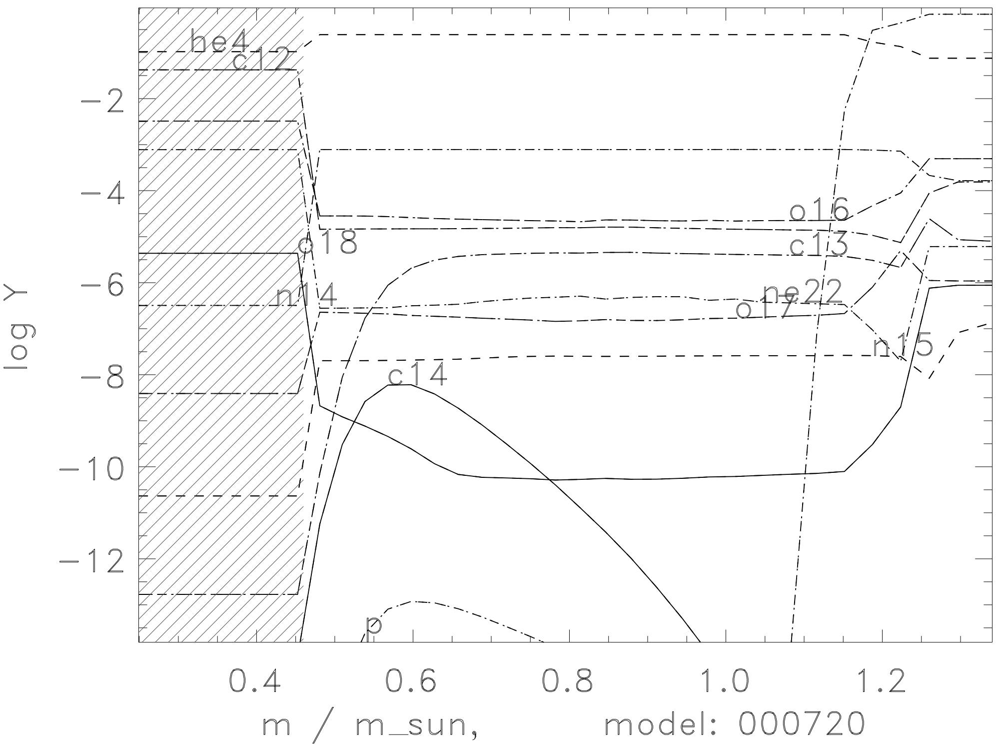

Fig. 2. Composition profile during core helium burning. The cross-hatched region shows the convective core.

the convective core the ^{13}C is destroyed by (α,n) and produces neutrons, which produce (n,p) reactions on ^{14}N as we saw above. Thus we see an increase in the ^{14}C and a concomitant increase in the proton abundance (see $M \simeq 0.6$). Moving further inward, to higher temperatures, we see the ^{14}C decay into ^{14}N reflected in the abunance profiles.

Figures 3 and 4 show the composition profiles near core helium exhaustion (these are presented in two figures for easier reading, with some key species such as hydrogen and helium repeated in both figures for orientation). The profiles in the core are easily understood: all helium has burned into ^{12}C and ^{16}O in the region which was the convective core, of $M = 0.5$ at its maximum extent. Further, the previously abundant ^{14}N ashes of hydrogen burning have suffered two alpha captures to produce ^{22}Ne. Number conservation demands that these both have the same mole fraction Y, as seen in the figure. There is also a small increase in the ^{26}Mg composition of the core due to the decay of the ^{26}Al[1] which was formed during the last (hottest) stages of hydrogen burning

[1] We always refer to the ground state of ^{26}Al unless otherwise explicitly stated.

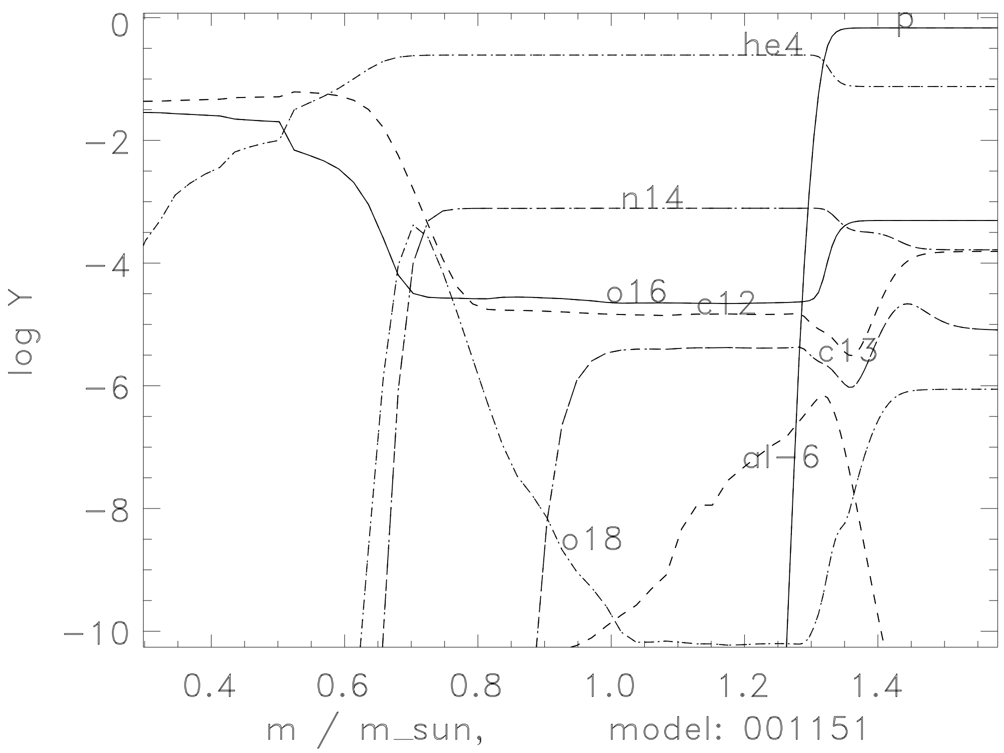

Fig. 3. Composition profiles at the time of core helium exhaustion.

from proton capture on ^{25}Mg, and also from alpha captures on ^{22}Ne near core helium exhaustion. (Note: ^{26}Al is denoted by "Al−6" in the figures, to distinguish it from the isomeric state.)

The hydrogen shell shows the expected abundance changes for CNO cycling. Note that a small amount of ^{26}Al is produced at the top of the shell (prior to its decay into ^{26}Mg in the lower half of the shell). The region between the bottom of the hydrogen shell and the helium exhausted core again shows the complete destruction of ^{13}C with the associated peak in ^{14}C and ^{18}O (a little further inward).

During the ascent of the early-AGB which follows core helium exhaustion, the hydrogen shell diminishes dramatically in strength, and the convective envelope moves further inward in mass. This is the second dredge-up phase. At its deepest, the envelope reaches down to $M = 0.91$. Thus we can use Figures 3 and 4 to explain the abundance changes seen during the second dredge-up.

The major surface abundance changes due to the second dredge-up are given in Table 1 above. Other minor changes are ^{20}Ne/^{21}Ne which increases from 15 to 16, ^{25}Mg/^{26}Mg which decreases from 0.87 to 0.75, and the ^{26}Al/^{27}Al ratio which rises from

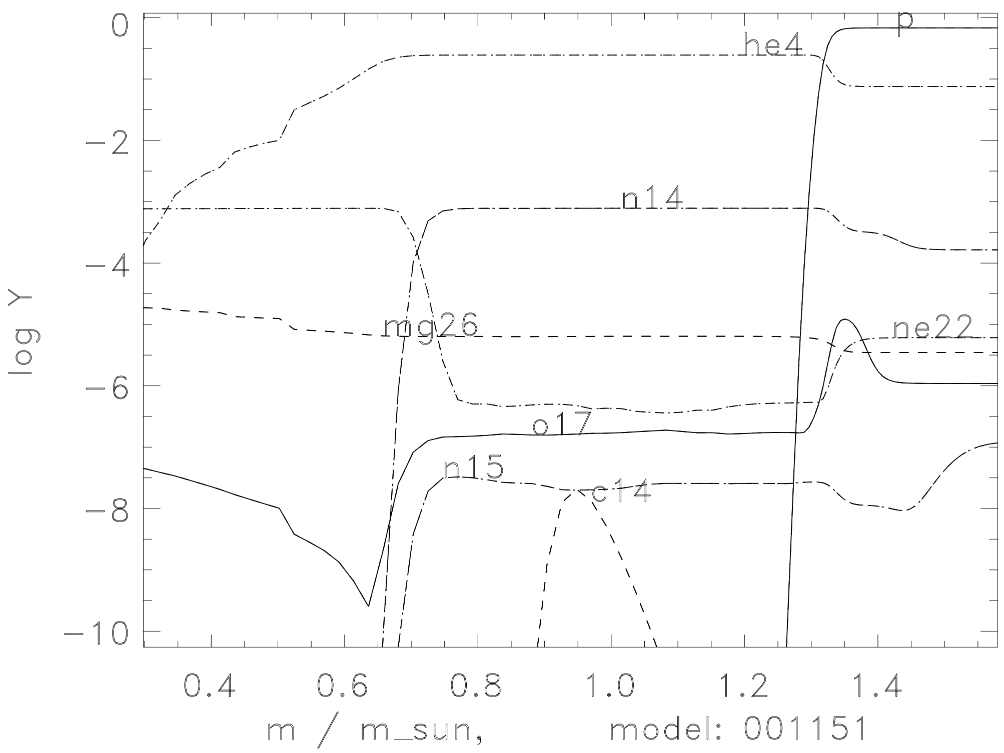

Fig. 4. Composition profiles at the time of core helium exhaustion.

zero to 0.002. It will rise further during the AGB evolution. Finally, the surface helium abundance by mass increases from 0.301 after first dredge-up to 0.356 after second dredge-up. (The initial value was 0.293 on the main sequence.)

4. Early AGB Evolution

After second dredge-up the hydrogen shell is re-ignited and is very thin. The outward progression of the helium shell continues until the two shells get physically close together and the first thermal pulse soon follows. Compositions just prior to the first thermal pulse are shown in Figure 5.

As is well known, at the thermal pulse the helium shell produces an enormous amount of energy ($L \simeq 10^7$ or $10^8\,\mathrm{L}_\odot$) which drives a convective pocket from the helium shell almost to the base of the hydrogen shell (for details see Frost and Lattanzio 1996b). Figure 6 shows the luminosity variation during the first few pulses.

The convective envelope, which moves inward following a pulse, doesn't penetrate the carbon-rich pocket (formed during the pulse) until the seventh pulse. Figure 7 shows the position of the inner edge of the convective envelope as well as the hydrogen and helium

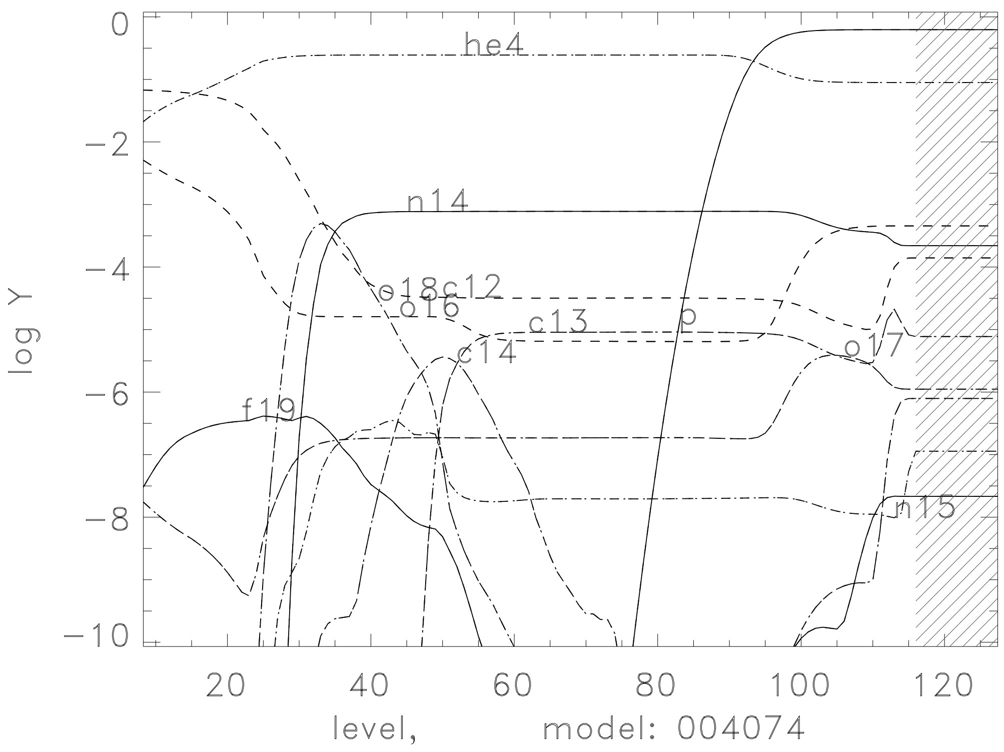

Fig. 5. Composition profiles just prior to the first pulse. Note that the x-axis is the level number, rather than the mass. This spreads the composition profiles so that both the hydrogen and helium shells can be viewed comfortably on the same axes. The helium shell extends from a mass of 0.910 to 0.912, and the hydrogen shell from 0.91415 to 0.91423.

shells during the first few pulses. Note that after a relatively small number of pulses, the dredge-up becomes very deep. It is common to define $\lambda = \Delta M_{dredge}/\Delta M_H$ = ratio of the mass dredged into the envelope to the amount of mass burned by the hydrogen shell during the interpulse phase. Typical values for λ are 0.3–0.6, increasing with mass. We note there that we soon find λ increasing toward unity. This is discussed further in Frost and Lattanzio (1996a). When this happens, the helium shell advances only a tiny amount at each pulse, as revealed in the figure.

In Figure 8 we show the variation of the surface abundances of selected species during the first seven pulses. Note that, as we have seen, the dredge-up does not reach into the carbon pocket during these early pulses. But it does reach into the region of material burnt by the hydrogen shell during the previous interpulse phase. To understand how this affects the surface abundances we will first look at the nucleosynthesis occurring

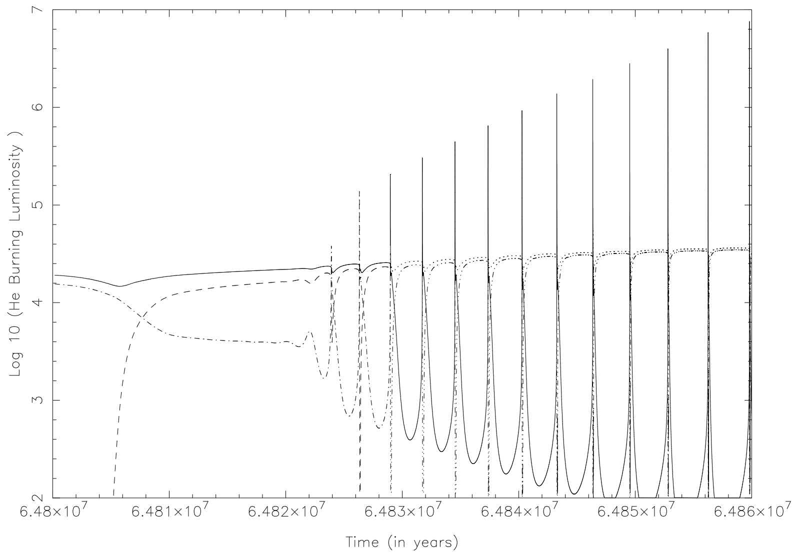

Fig. 6. Variation of selected luminosities during the first few pulses. The solid line represents the total luminosity, the dashed line is for hydrogen burning, and the short-dashed line is for helium burning.

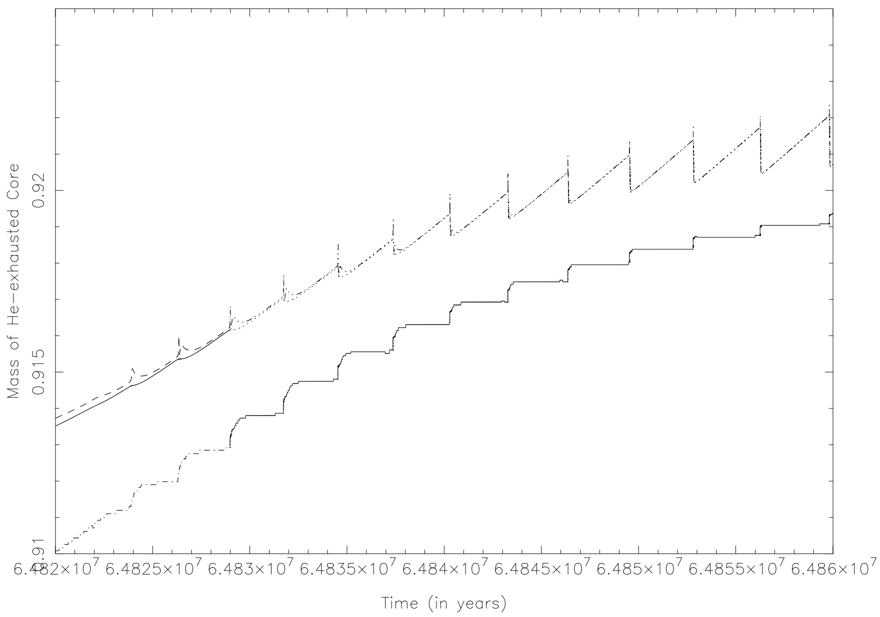

Fig. 7. Variation of the inner edge of the convective envelope (top line) together with the position of the hydrogen shell (next line, usually on top of the previous line) and the position of the helium shell. All are measured in solar masses.

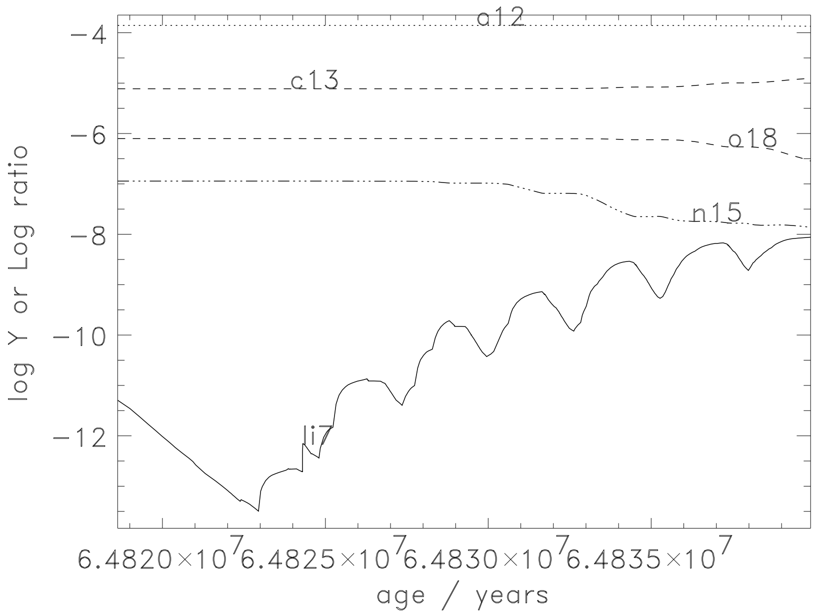

Fig. 8. Variation of the surface abundances of selected species during the first seven thermal pulses. Note the dramatic increase in ^{7}Li.

during a thermal pulse, and the resultant composition profiles.

5. The Seventh Thermal Pulse

5.1. The Hydrogen Shell

Firstly we look at the region below the convective envelope, including the hydrogen shell, but above the intershell convective pocket (which we discuss below). The profiles in this region are typical of the action of the CNO cycles, and have been discussed before. Changes in envelope composition are due to the action of HBB during the interpulse phase of even these early pulses, *prior* to dredge-up. We see a decrease of ^{18}O which is almost totally destroyed in the hydrogen shell. Likewise, this explains the increase in ^{7}Li seen in the figure[2], which has been explained by Boothroyd and Sackmann 1992 as being due to the Cameron-Fowler Beryllium Transport mechanism. HBB is also responsible for the decrease in ^{15}N seen in Figure 8. This is due to the substantial CN cycling which occurs at the very bottom of the envelope. Figure 9 shows the reaction rates at a point near the bottom, but within, the convective envelope. We see the CN cycling which produces ^{13}C from ^{12}C, and destroys the ^{15}N, both of which effects are clearly seen in Figure 8. One can also see the production of ^{7}Li, but we do not discuss this in detail as it has been adequately covered by Boothroyd and Sackmann (1992; see also Frost and

[2] Note that we have truncated our reaction rates at $T = 8 \times 10^6$K, which is of negligible effect for most species, but does result in a value for the ^{3}He abundance which is perhaps a factor of 2 or 3 too small, and that this translates into a similar underestimate for our ^{7}Li abundance.

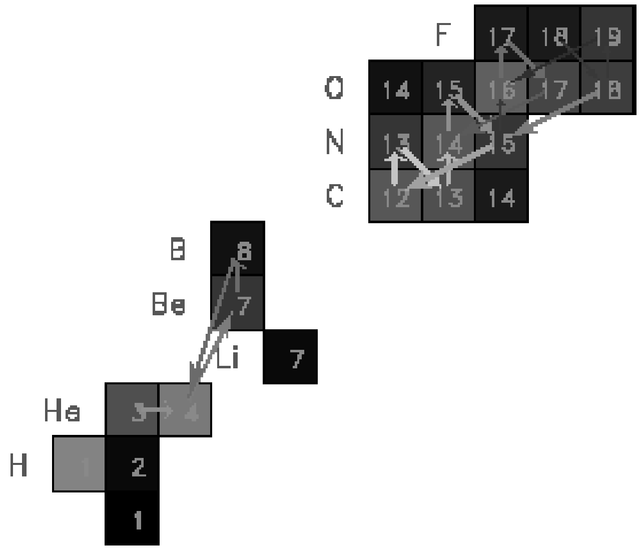

Fig. 9. Reaction rates for the mass region at the bottom of the convective envelope in a typical interpulse phase of an early pulse. The boxes are coloured according to the abundance of the species they represent (black means mole fraction is zero), and the arrows are coloured and thickened according to the rate of the reaction: thicker, lighter arrows mean a faster reaction than thinner, darker arrows. Likewise, the colour of the square repsenting a particular isotope is lighter for a higher abundance and draker for a lower abundance.

Lattanzio 1996b).

5.2. The Convective Pocket

At the peak of the pulse, the strong helium burning produces a convective pocket which reaches almost to the hydrogen shell. This mixes the products of helium burning (mostly ^{12}C) throughout the intershell region, and when the convective envelope next penetrates this region during dredge-up, the products of this nucleosynthesis are mixed to the surface. In Figure 10 we show the compositions within the convective shell just after the peak of the seventh pulse. Note that at its maximum extent the convection covered the approximate region 0.9167 to 0.9191. The convection has receded slightly in the model shown in the figure, and we do not show the bottom of the convective region.

Within the convective pocket we see the triple-alpha reactions producing ^{12}C primarily, with almost no ^{16}O, as is expected from only partial helium burning. Rather, there is a relatively large amount of ^{22}Ne which has resulted from consecutive alpha captures on ^{14}N. This also keeps the ^{18}O composition quite low. Also produced in the intermediate zone is ^{19}F from alpha captures on ^{15}N. Reaction rates for the zone at mass 0.9168, near the bottom of the convective zone, are shown in Figure 12.

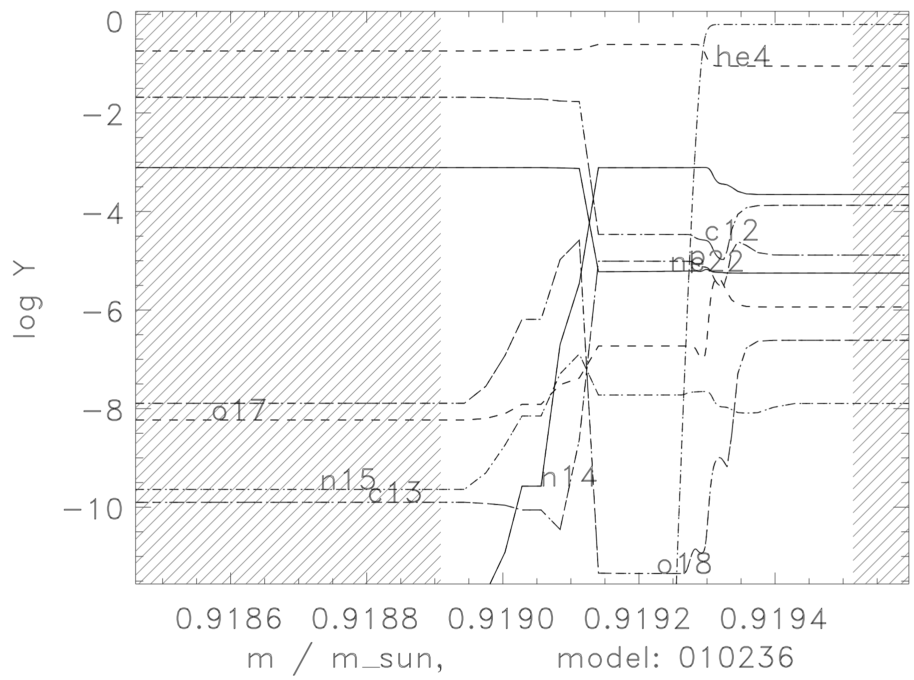

Fig. 10. Composition profiles during the seventh pulse. We show the region between the convective pulse and the bottom of the convective envelope.

Finally, note that there is a steep gradient in the ^{18}O abundance just above the convective pocket shown in Figure 10. This reflects a similar gradient in ^{14}C and more importantly, ^{14}N. Remember, the convection initially extends out to 0.9191, which marks the peak of these profiles. When the convection reaches this far it engulfs the ^{14}N profile left from previous evolution, and then this burns by alpha capture to produce ^{22}Ne. Thus the varying profile of these elements results from their destruction as the convection recedes, leaving behind material poorer and poorer in these species.

6. Advanced AGB Evolution

6.1. Envelope Temperature and the Dredge-up

As the star ascends the AGB the temperature at the base of the convective envelope increases dramatically, reaching values of up to 82 million K, as shown in Figure 13. Soon after this, however, the temperature begins to decrease due to the effects of mass loss (included here via the prescription of Vassilliadis and Wood 1993). As the envelope mass decreases the HBB is shutdown, long before the third dredge-up ends. The details of the surface composition in the latter stages of a star's life depend critically on the competition between these effects (e.g. Groenewegen and deJong 1993). Here we find that a natural result of our models is that the HBB ceases, but that dredge-up continues.

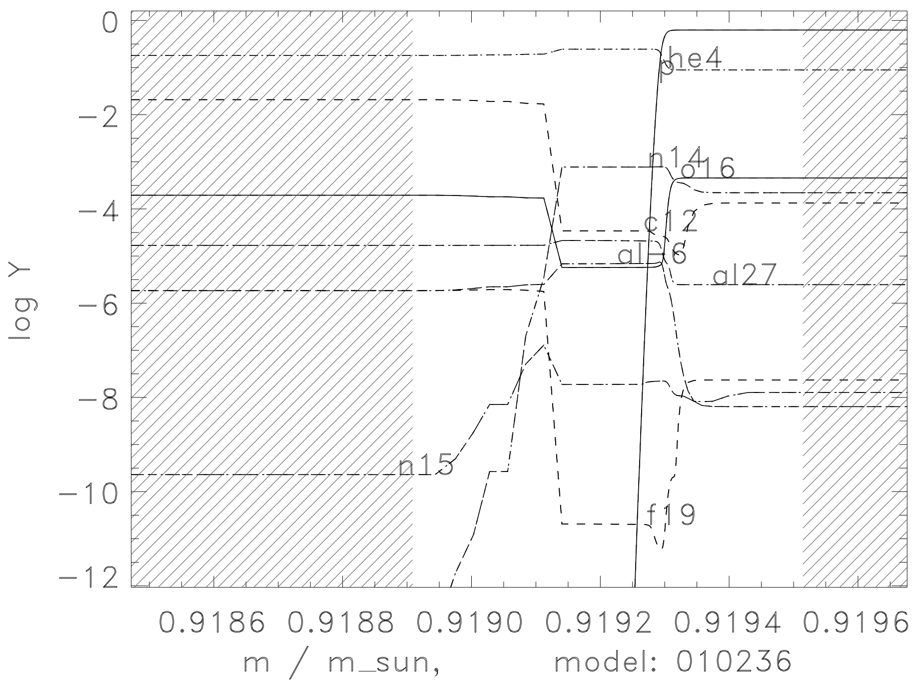

Fig. 11. Same as Figure 10, but showing some different species.

Indeed, the dredge-up is still strong at the 43rd pulse (when the mass has been reduced to 2.4) when we stopped calculations due to convergence problems. This is shown in Figure 14. Thus, for most of its lifetime on the AGB, it may be possible for HBB to prevent a star from becoming a carbon star. Yet, when HBB is shut down due to mass loss the recurring third dredge-up may yet produce a carbon star. But now it will be one with many characteristics of HBB (except for the equilibrium $^{12}C/^{13}C$ ratio, of course). We will address this in a later paper. But for now we shall look in more detail at the nucleosynthesis which occurs between the 30th and 31st pulses, which is representative of a typical interpulse phase spent undergoing substantial HBB.

6.2. Nucleosynthesis by HBB

In the deepest layer of the convective envelope the temperatures are about 82 million K, and there is substantial hydrogen burning via the CNO cycle. Initially the $^{12}C/^{13}C$ ratio is out of equilibrium because of the ^{12}C added to the envelope by the previous dredge-up episode. Thus initially the ^{13}C rises and ^{12}C falls as these come into equilibrium. The convective turnover timescale is such that the entire envelope passes through the hot bottom of the envelope many times during the interpulse phase, and the entire envelope receives the equilibrium abundances of ^{12}C and ^{13}C. Then both carbon isotopes fall in concert as they are processed further into ^{14}N. Further, at these high temperatures ^{26}Mg suffers substantial proton captures and produces ^{27}Al during the interpulse phase. Also, the ^{19}F which is produced in the convective shell during pulses, and then dredged

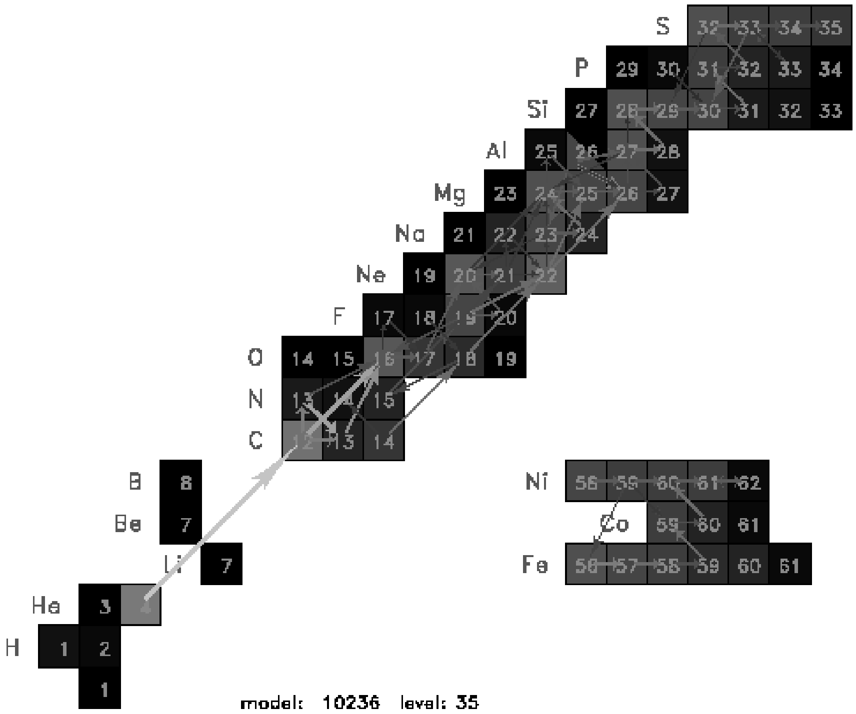

Fig. 12. Reaction rates at $M = 0.9168$, at the bottom of the convective pocket of the seventh pulse.

to the surface, is destroyed by (p,α) reactions.

6.3. Nucleosynthesis Below the Envelope

Figure 15 shows the composition profiles just above the hydrogen shell in a model which is just beyond the 30th pulse. Figure 16 shows the same region (on the same scale) for a model which is just approaching the 31st pulse. Thus these two figures represent models at the start and finish of the interpulse phase, between the 30th and 31st pulses. The hatched region denotes convection, and hence the position of the hydrogen shell. Thus these pictures show how far the hydrogen shell moves during the interpulse phase, and also reveals what happens to the hydrogen ashes left behind by the shell.

Firstly look at the ^{13}C profile. It leaves the hydrogen shell with $\log Y_{13} \simeq -4.9$, yet during the interpulse phase this burns totally via alpha captures, with a subsequent increase in the ^{16}O abundance, as seen in Figure 16. This was seen first in low mass stars by Straniero et al (1995 and then verified in more massive stars by Mowlavi et al (1996). Some of the neutrons so released are absorbed on the abundant ^{14}N (not shown) to produce ^{14}C via (n,p) reactions, as discussed above. This ^{14}C also captures an alpha particle to produce the ^{18}O bump seen in Figure 16. This will be absorbed

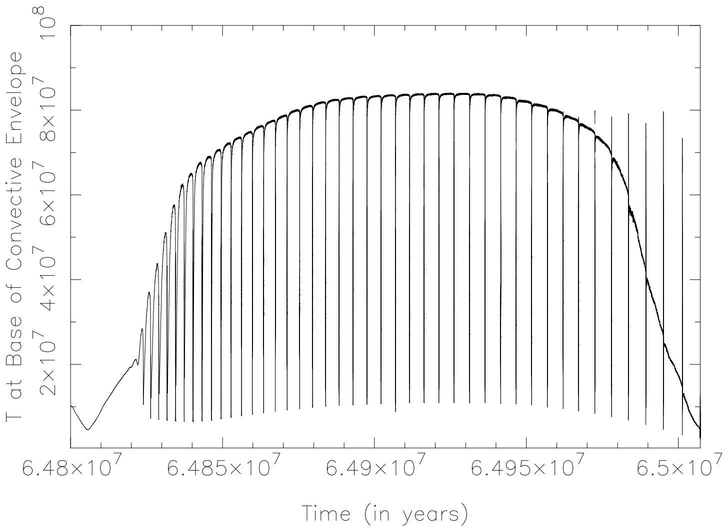

Fig. 13. Temperatures at the base of the convective envelope during the AGB evolution for the first 43 pulses.

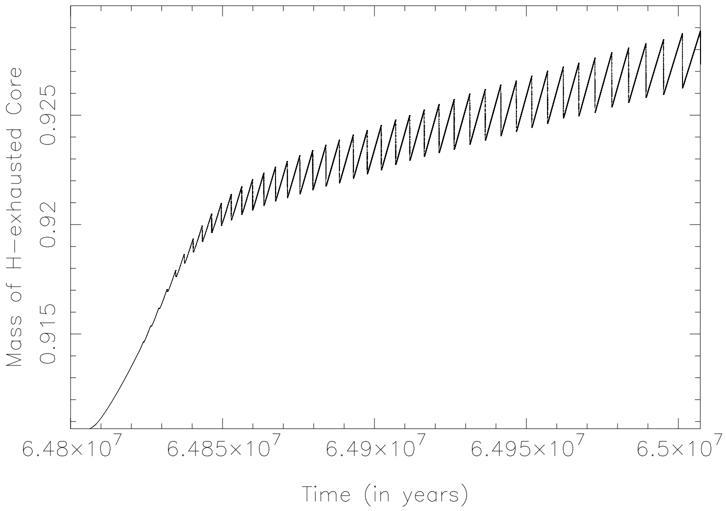

Fig. 14. Position of the hydrogen exhausted core during the same time span as figure 13.

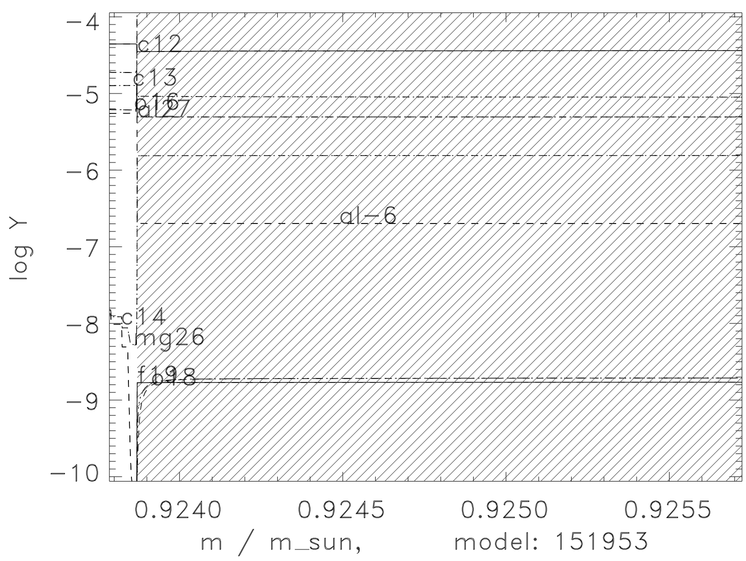

Fig. 15. Compositions in a model near the start of the interpulse phase. The hatched region represents convection. Note that this figure complements Figure 16.

by the next thermal pulse, to produce ^{22}Ne and hence neutrons. The neutron capture nucleosynthesis will be the subject of a subsequent paper.

The hydrogen shell also produces ^{27}Al. This is present at the level $\log Y_{27} \simeq -5.3$ in the envelope in Figure 15, and it rises to -4.7 interior to the hydrogen shell, due to the proton captures on ^{26}Mg which occur there. But note from Figure 16 that as the hydrogen shell advances during the interpulse, it leaves behind a profile with $\log Y_{27} \simeq -4.7$. When this material is added to the envelope after the next dredge-up phase it will enhance the surface composition of ^{27}Al. Hence we see that there are two effects which produce the increase in surface ^{27}Al in AGB stars: both dredge-up and HBB. Finally, note that ^{19}F is destroyed during its passage through the hydrogen shell, and Figure 15 shows that it diminishes to the value $\log Y_{19} \simeq -10.5$. But during the interpulse phase it is produced via proton capture on ^{18}O and gradually climbs to the value of $\log Y_{27} \simeq -7.8$ revealed in Figure 16.

6.4. Surface Composition Changes

We conclude by showing the surface composition changes calculated for the first 43 pulses of the $6\,\mathrm{M}_{\odot}$ model described above. Figure 17 shows the variation of the CNO species. (The discontinuities in the curves show the effect of dredge-up, while the gradual changes between the discontinuities are due to HBB.) The carbon isotopes have been discussed above, and the only feature worthy of further comment is that as the HBB ceases, we see the ^{12}C abundance begins to increase again, and the isotopic ratio now differs

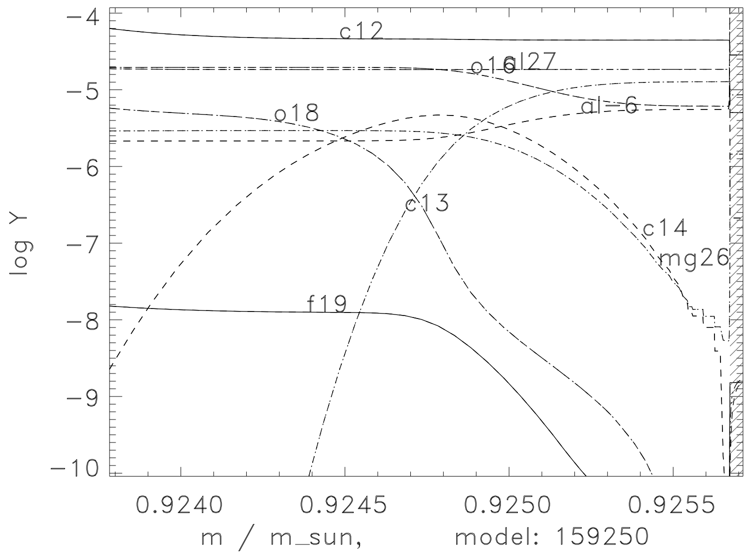

Fig. 16. Compositions in a model near the end of the interpulse phase. The hatched region represents convection. Note that this figure complements Figure 15.

substantially from its equilibrium value (see also Figure 19). The increase in ^{14}N from CN cycling is quite apparent, and a small decrease in the ^{16}O content is just visible on the scale of the diagram. As we have seen earlier, the ^{18}O is almost completely destroyed within the envelope as soon as HBB begins. Likewise, ^{15}N is seen in equilibrium with ^{14}N for most of the evolution, but this breaks down when HBB ceases (just as happened for the carbon isotopes). Note that there is an order of magnitude increase in the ^{17}O abundance during the AGB evolution.

In Figure 18 we show some other species of interest including ^{7}Li and ^{3}He whose fates are connected. The ^{7}Li content increases very quickly once HBB begins, and then starts to decrease once the ^{3}He begins to be depleted significantly. The luminosity range and duration of the super-Li-rich phase has been shown by Boothroyd and Sackmann (1992) to fit the observations very well. We also see in this figure the production of ^{25}Mg, ^{26}Al and ^{27}Al, all due to the operation of the Mg-Al cycle both in the envelope as well as in the hydrogen shell, and their subsequent dredge-up. Note that the envelope ^{26}Mg content initially decreases, due to HBB, but then rises again once the HBB is turned off and dredge-up dominates.

Finally in Figure 19 we show the ratios of selected species during the same evolutionary phase as shown in the previous two figures. A comparison with stellar and meteoritic abundances will be included in a later paper, but we already see that the high ^{26}Al/^{27}Al ratio of up to 0.05 is in good agreement with the most ^{26}Al-rich meteorite grains which reach values of up to 0.1 (Zinner 1994). Finally, note that the ratio of ^{19}F/^{16}O initially increases slightly (as ^{19}F is made in the convective shell and dredged to the surface) but

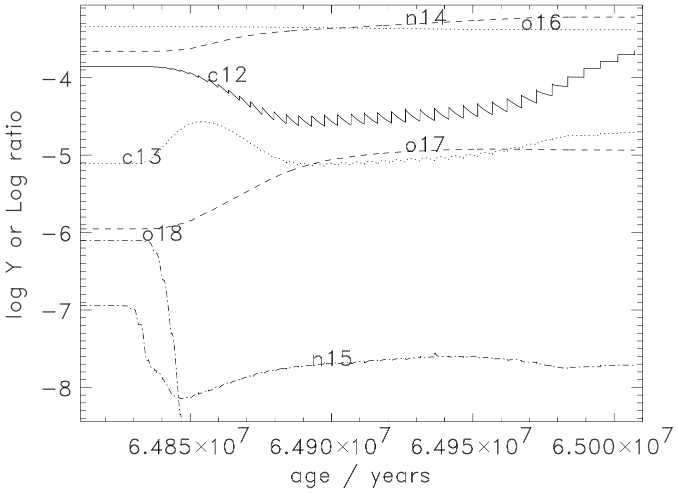

Fig. 17. Time variation of surface abundances of selected species during the thermally pulsing evolution.

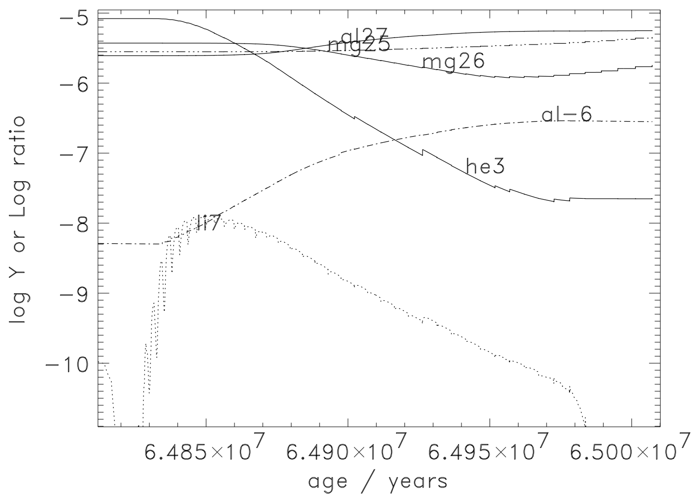

Fig. 18. Time variation of surface abundances of selected species during the thermally pulsing evolution.

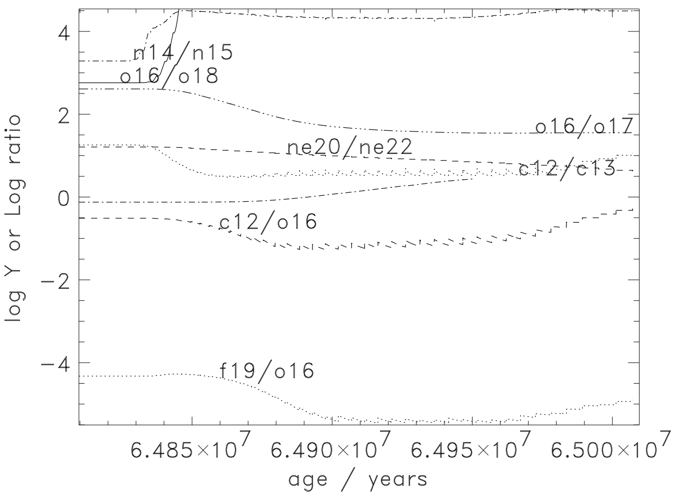

Fig. 19. Time variation of selected isotopic ratios in the envelope of the model during the thermally pulsing evolution.

later decreases due to HBB destroying the ^{19}F. Thus it would appear that stars experiencing HBB should not show increases of both ^{19}F and ^{7}Li simultaneously. However, as the HBB is turned off by the mass loss, the ^{19}F abundance begins to increase again, due to dredge-up. A detailed analysis of the variation of ^{19}F has been carried out by Mowlavi et al (1996), to whom we defer for details.

7. Conclusions

We have presented a brief summary of the nucleosynthesis (and an ever briefer summary of the evolution) of a model star of $6\,M_\odot$ with $Z = 0.02$. We find substantial dredge-up occurs, naturally, and becomes very deep, with dredge-up parameter λ approaching unity. With a new nucleosynthesis code we have calculated the detailed processing during the first 43 pulses of the star, and have found that the model matches quite well many known constraints (e.g. first and second dredge-up isotopic ratios). Further, during the AGB evolution a combination of dredge-up and HBB leads to many surface composition changes. A full analysis of this model, as well as eight others, will form the subject of later papers.

Acknowledgements

We would like to thank Arnold Boothroyd and Roberto Gallino for many useful discussions. Also, the patience of the editors is appreciated, and we wish to thank the organisers for producing such a stimulating meeting. This work was supported by the Australian Research Council.

References

Arnould, M., Mowlavi, N., and Champagne, A.: in *"Stellar Evolution: What Should Be Done?"*, Proceedings of the 32nd Liege Colloquium, Eds A. Noels et al, 17.
Boothroyd, A.I., and Sackmann, I.-J.: 1992 *Astrophys. J. Lett.* **393**, LL21.
Cameron, A.G.W., and Fowler, W.A.: 1971 *Astrophys. J.* **164**, 111.
Cannon, R.C.: 1993 *Mon. Not. R. Astr. Soc.* **263**, 817.
Cannon, R.C., Frost, C.A., Lattanzio, J.C., and Wood, P.R.: 1996 (in preparation).
Frost, C.A. and Lattanzio, J.C.: 1996a (submitted).
Frost, C.A. and Lattanzio, J.C.: 1996b in *"Stellar Evolution: What Should Be Done?"*, Proceedings of the 32nd Liege Colloquium, Eds A. Noels et al, 307.
Groenewegen, M.A.T. and de Jong, T.: 1993 *Astron. Astrophys.* **267**, 410.
Jorissen, A., and Arnould, M.: 1989 *Astrophys. J.* **221**, 161.
Käppeler, F. et al 1994: *Astrophys. J.* **437**, 396.
Lattanzio, J.C.: 1986 *Astrophys. J.* **311**, 708.
Mowlavi, N., Jorissen, A. and Arnould, M.: 1996 (preprint).
Rogers, F.J. and Iglesias, C.A.: 1992 *Astrophys. J. Suppl.* **79**, 507.
Smith, V.V. and Lambert, D.L.: 1989 *Astrophys. J.* **345**, 375.
Straniero, O., et al: 1995*Astrophys. J. Lett.* **440**, LL85.
Thielemann, F.-K., Arnould, M., and Truran, J.W.: 1987 in *"Advances in Nuclear Astrophysics"* Eds E. Vangioni-Flam et al, Editions Frontiers, Gif-sur-Yvette, 525.
Vassilliadis, E. and Wood, P.R.: 1993 *Astrophys. J.* **413**, 641.
Wood, P.R.: 1981 *Astrophys. J.* **248**, 311.
Wood, P.R., Bessell, M.S., and Fox, M. W.: 1983 *Astrophys. J.* **272**, 99.
Zinner, E.K.: 1995 in *Nuclei inthe Cosmos III* Eds M. Busso, R. Gallino and C. M. Raiteri, (AIP Press: New York), 567.